

Thermodynamic properties of nano-silver and alloy particles

Wangyu Hu, Shifang Xiao, Huiqiu Deng,
Wenhua Luo and Lei Deng

*Department of Applied Physics, Hunan University, Changsha 410082,
PR China*

In this chapter, the analytical embedded atom method and calculating Gibbs free energy method are introduced briefly. Combining these methods with molecular dynamic and Monte Carlo techniques, thermodynamics of nano-silver and alloy particles have been studied systematically.

For silver nanoparticles, calculations for melting temperature, molar heat of fusion, molar entropy of fusion, and temperature dependences of entropy and specific heat capacity indicate that these thermodynamic properties can be divided into two parts: bulk quantity and surface quantity, and surface atoms are dominant for the size effect on the thermodynamic properties of nanoparticles.

Isothermal grain growth behaviors of nanocrystalline Ag shows that the small grain size and high temperature accelerate the grain growth. The grain growth processes of nanocrystalline Ag are well characterized by a power-law growth curve, followed by a linear relaxation stage. Beside grain boundary migration and grain rotation mechanisms, the dislocations serve as the intermediate role in the grain growth process. The isothermal melting in nanocrystalline Ag and crystallization from supercooled liquid indicate that melting at a fixed temperature in nanocrystalline materials is a continuous process, which originates from the grain boundary network. The crystallization from supercooled liquid is characterized by three characteristic stages: nucleation, rapid growth of nucleus, and slow structural relaxation. The homogeneous nucleation occurs at a larger supercooling temperature, which has an important effect on the process of crystallization and the subsequent crystalline texture. The kinetics of transition from liquid to solid is well described by the Johnson-Mehl-Avrami equation.

By extrapolating the mean grain size of nanocrystal to an infinitesimal value, we have obtained amorphous model from Voronoi construction. From nanocrystal to amorphous state, the curve of melting temperature exhibits three characteristic regions. As mean grain size above about 3.8 nm for Ag, the melting temperatures decrease linearly with the reciprocal of grain size. With further decreasing grain size, the melting temperatures almost keep a constant. This is because the dominant factor on melting temperature of nanocrystal shifts from grain phase to grain boundary one. As a result of fundamental difference in structure, the amorphous has a much lower solid-to-liquid transformation temperature than that of nanocrystal.

The surface and size effects on the alloying ability and phase stability of Ag alloy nanoparticles indicated that, besides the similar compositional dependence of heat of formation as in bulk alloys, the heat of formation of alloy nanoparticles exhibits notable size-dependence, and there exists a competition between size effect and compositional effect on the heat of formation of alloy system. Contrary to the positive heat of formation for bulk immiscible alloys, a negative heat of formation may be obtained for the alloy nanoparticles with a small size or dilute solute component, which implies a promotion of the alloying ability and phase stability of immiscible system on a nanoscale. The surface segregation results in an extension of the size range of particles with a negative heat of formation.

1. Thermodynamic properties of silver nanoparticles

Nanoparticle systems currently attract considerable interest from both academia and industry because of their interesting and diverse properties, which deviate from those of the bulk. Owing to the change of the properties, the fabrication of nanostructural materials and devices with unique properties in atomic scale has become an emerging interdisciplinary field involving solid-state physics, chemistry, biology, and materials science. Understanding and predicting the thermodynamics of nanoparticles is desired for fabricating the materials for practical applications.¹ The most striking example of the deviation of the corresponding conventional bulk thermodynamic behavior is probably the depression of the melting point of small particles of metallic species. A relation between the radius of nanoparticles and melting temperature was first established by Pawlow,² and the first experimental investigation of melting-temperature dependence on particle size was conducted more than 50 years ago.³ Further studies were performed by a great number of researchers.⁴⁻¹² The results reveal that isolated nanoparticles and substrate-supported nanoparticles with relatively free surfaces usually exhibit a significant decrease in melting temperature as compared with the corresponding conventional bulk materials. The physical origin for this phenomenon is that the ratio of the number of surface-to-volume atoms is enormous, and the liquid/vapor interface energy is generally lower than the average solid/vapor interface energy.⁹ Therefore, as the particle size decreases, its surface-to-volume atom ratio increases and the melting temperature decreases as a consequence of the improved free energy at the particle surface.

A lot of thermodynamic models of nanoparticles melting assume spherical particles with homogeneous surfaces and yield a linear or almost linear decreasing melting point with increasing the inverse of the cluster diameter.^{2,6,10-12} However, the determination of some parameters in these models is difficult or arbitrary. Actually, the melting-phase transition is one of the most fundamental physical processes. The crystal and liquid phases of a substance can coexist in equilibrium at a certain temperature, at which the Gibbs free energies of these two phases become the same. The crystal phase has lower free energy at a temperature below the melting point and is the stable phase. As the temperature goes above the melting point, the free energy of the crystal phase becomes higher than that of the liquid phase and phase transition will take place. The same holds true for nanoparticles. We have calculated the Gibbs free energies of solid and liquid phases for silver bulk material and its surface free energy using molecular dynamics with the modified analytic embedded-atom method (MAEAM). By representing the total Gibbs free energies of solid and liquid clusters as the sum of the central bulk and surface free energy,^{5,13,14} we can attain the free energies

for the liquid and solid phase in spherical particles as a function of temperature. The melting temperature of nanoparticles is obtained from the intersection of these free-energy curves. This permits us to characterize the thermodynamic effect of the surface atoms on size-dependent melting of nanoparticles and go beyond the usual phenomenological modeling of the thermodynamics of melting processes in nanometer-sized systems. In addition, we further calculate the molar heat of fusion, molar entropy of fusion, entropy, and specific heat capacity of silver nanoparticles based on free energy calculation.

In order to explore the size effect on the thermodynamic properties of silver nanoparticles, we first write the total Gibbs free energy G^{total} of a nanoparticle as the sum of the volume free energy G^{bulk} and the surface free energy $G^{surface}$

$$G^{total} = G^{bulk} + G^{surface} = Ng(T) + \gamma(T)A_s \tag{1}$$

The detailed description on calculation of G^{bulk} and $G^{surface}$ has been given in Ref. 15-17. Assuming a spherical particle leads to a specific surface area of^{5,10,18}

$$A_s = \frac{6}{D} N v_{at}(T) \tag{2}$$

where N is the total number of atoms in the particle, D is the radius of the particle, and $v_{at}(T)$ is the volume per atom. Second-order polynomials are adjusted to the simulation results of the internal energy for the solid and liquid phase shown in Fig. 1. The Gibbs free energies per atom for the solid and liquid phase are written as

$$g(T) = g(T_0)(T / T_0) - T[a_2(T - T_0) + a_1 \ln(T / T_0) - a_0(1 / T - 1 / T_0)] \tag{3}$$

where a_i are the polynomial coefficients, resulting from molecular dynamics (MD) simulations.¹⁷

The surface free energy of a solid spherical particle may be determined by the average surface free energy of the crystallite facets and the Gibbs–Wulff relation¹⁹

$$\sum_i A_i \gamma_{si} = \text{minimum} \tag{4}$$

The equilibrium crystal form develops so that the crystal is bound by low surface energy faces in order to minimize the total surface free energy.²⁰ For two surfaces i and j at equilibrium, $A_i \gamma_i = A_j \gamma_j = \mu$, where μ is the excess chemical potential of surface atoms relative to interior atoms. A surface with higher surface free energy (γ_i) consequently has a smaller surface area (A_i), which is inversely proportional to the surface free energy. Accordingly, the average surface free energy of the crystal, weighted by the surface area, is

$$\gamma_s = \frac{\sum_{i=1}^n A_i \gamma_{si}}{\sum_{i=1}^n A_i} = \frac{\sum_{i=1}^n \frac{\mu}{\gamma_i} \gamma_{si}}{\sum_{i=1}^n \frac{\mu}{\gamma_{si}}} = \frac{n}{\sum_{i=1}^n \frac{1}{\gamma_{si}}} \tag{5}$$

where n is the number of facets under consideration. Each crystal has its own surface energy, and a crystal can be bound by an infinite number of surface types. Thus, we only consider three low index surfaces, (111), (100), and (110), because of their low surface energies, and the surface free energy γ_i of the facet i is calculated as follows

$$\gamma_i(T) = \gamma_i(T_0) \frac{T}{T_0} - T[b_{2i}(T - T_0) + b_{1i} \ln(\frac{T}{T_0}) - \frac{b_{0i}}{T} + \frac{b_{0i}}{T_0}] \tag{6}$$

where b_{ki} ($k = 0,1,2$) are the coefficients for the surface free-energy calculation for facet i , and

$\gamma_i(T_0)$ is surface free energy at the reference temperature T_0 .¹⁷ On the basis of the expression for the Gibbs free energy, general trends for thermodynamic properties may be deduced. For example, the melting temperature T_m for nanoparticles of diameter D can be obtained by equating the Gibbs free energy of solid and liquid spherical particles with the assumption of constant pressure conditions, and temperature and particle size dependence of the entropy per atom for solid nanoparticles can then be defined using the following expression

$$s^s(T, D) = -\left(\frac{\partial g^s}{\partial T}\right)_p$$

$$= 2a_2^s T + a_1^s \ln\left(\frac{T}{T_0}\right) - \frac{g^s(T_0)}{T_0} - a_2^s T_0 + a_1^s + \frac{a_0^1}{T_0} - \frac{2v_{at}(T)(\gamma^s)^2}{D} \sum_{i=1}^3 \frac{\gamma_i'}{\gamma_i^2} \quad (7)$$

where the primes denote derivatives with regard to temperature. The contribution from the derivative of atomic volume is trivial; it is reasonable to neglect. Using the relation between the specific heat capacity at constant pressure and the entropy, we can write the expression for the specific heat capacity per mole as

$$C_p^s(T, D) = N_0 T \left(\frac{\partial s^s}{\partial T}\right)_p$$

$$= 2N_0 a_2^s T + N_0 a_1^s - \frac{6N_0 T v_{at}(T)}{D} \left\{ \frac{2}{\gamma^s} [(\gamma^s)']^2 + \frac{(\gamma^s)^2}{3} \sum_{i=1}^3 \left[\frac{\gamma_i''}{\gamma_i^2} - \frac{2(\gamma_i')^2}{\gamma_i^3} \right] \right\} \quad (8)$$

where N_0 is Avogadro's number. The internal energy per atom for nanoparticles can be written as^{5,10}

$$h_{v,D}(T, D) = h_v(T) + \frac{6v_{at}(T) \gamma(T)}{D} \quad (9)$$

where h_v represents the internal energy per atom of bulk material. The molar heat of fusion and molar entropy of fusion for nanoparticles can be derived from the internal energy difference of solid and liquid nanoparticles easily.

$$\Delta H_m = N_0 \left[h_{v,D}^l(T_m, D) - h_{v,D}^s(T_m, D) \right]$$

$$= \Delta H_{mb} \left[1 - \frac{6v_{at}^s(T_m)}{LD} (\gamma^s(T_m) - \gamma^l(T_m) \frac{v_{at}^l(T_m)}{v_{at}^s(T_m)}) \right] \quad (10)$$

$$= \Delta H_{mb} \left[1 - \frac{\beta_1(T_m)}{D} \right]$$

where ΔH_{mb} is the molar heat of fusion for bulk, and L is the latent heat of melting per atom. The superscript "s" and "l" represent solid phase and liquid phase, respectively.

Figure 1 shows the behavior of the solid and liquid internal enthalpies as a function of temperature, and an abrupt jump in the internal energy during heating can be observed, but this step does not reflect the thermodynamic melting because periodic boundary condition calculations provide no heterogeneous nucleation site, such as free surface or the solid-liquid interface, for bulk material leading to an abrupt homogeneous melting transition at about 1500 K (experimental melting point 1234 K), as it is revealed that the confined lattice without free surfaces can be significantly superheated.²¹ The latent heat of fusion is 0.115 eV/atom, in good agreement with the experimental value of 0.124 eV/atom.²²

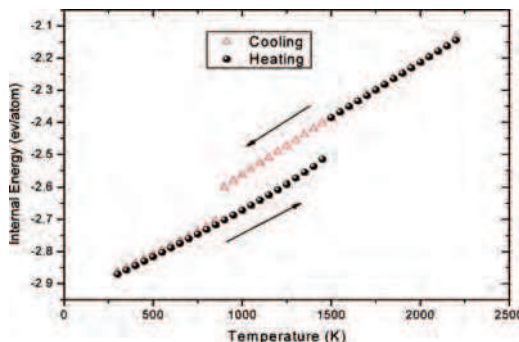


Fig. 1. Internal energy as a function of temperature for bulk material. Heating and cooling runs are indicated by the arrows and symbols. (Picture redrawn from Ref. 17)

The free-energy functions for the solid and liquid phases have been plotted in Fig. 2. The melting temperature T_{mb} is obtained from the intersection of these curves. From Fig. 2, two curves cross at $T_{mb}=1243$ K, which is in good agreement with the experimental melting point $T^{exp}=1234$ K. The good agreement in melting point is consistent with accurate prediction of the Gibbs free energies.

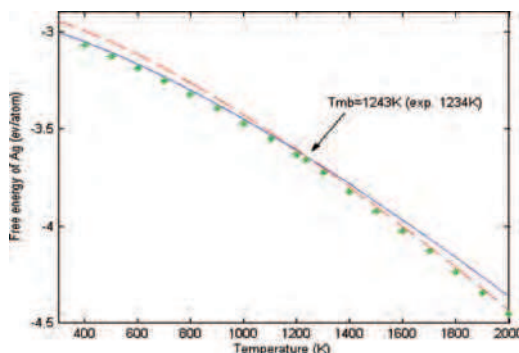


Fig. 2. Gibbs free energy of the solid and liquid phase in units of eV/atom. The asterisks denote the experimental values²². The solid curve is the MAEAM solid free energy, and the dashed curve is the MAEAM liquid free energy. The temperature at which Gibbs free energy of the solid and liquid phase is identical is identified as the melting point. (Picture redrawn from Ref. 17)

The calculation results of solid surface free energy for the (111), (100), and (110) surfaces with thermodynamic integration approach (TI)²³ is depicted in Fig. 3. It can be seen that the free energies of the surfaces at low temperatures are ordered precisely as expected from packing of the atoms in the layers. The close-packed (111) surface has the lowest free energy, and loosely packed (110) the largest. As temperature increases, the anisotropy of the surface free energy becomes lower and lower because the crystal slowly disorders. For comparison, we also utilize Grochola et al’s “simple lambda” and “blanket lambda” path (BLP)^{24,25} to calculate the solid surface free energy for the three low-index faces. The results are in good

agreement with the TI calculation for temperature from 300 to 750 K. As an example, the simulation results for the integrand $\langle \partial E(\lambda) / \partial \lambda \rangle_\lambda + \langle \partial \varphi_{\text{rep}}^{\text{AB}} / \partial \lambda \rangle_\lambda$ for the (110) face at 750 K is shown in Fig. 4. It is obvious that the results are very smooth and completely reversible. In order to create the slab, we also show the expansion process using z-density plots for $(L_z - L_z^0) / L_z^0 = 0, 0.045, \text{ and } 0.08$, in Fig. 5. At $(L_z - L_z^0) / L_z^0 = 0.08$, the adatoms appearing between A and B sides can be seen. According to Grochola et al.,²⁵ it indicates that the BLP samples the rare events more efficiently than the cleaving lambda method²⁶ because the two surfaces interact via the adatoms when separated, as seen in Fig. 5. These adatoms would tend to have greater fluctuations in the z direction interacting with each other than if they were interacting with a static cleaving potential. They should therefore be more likely to move onto other adatoms sites or displace atoms underneath them, which should result in better statistics. The work obtained from the system in this expansion is roughly 5% of the work put into the system in the first part. For comparison, ab initio calculation results at $T=0$ K performed by L. Vitos et al. adopting the FCD method²⁷ is shown in Fig. 3.

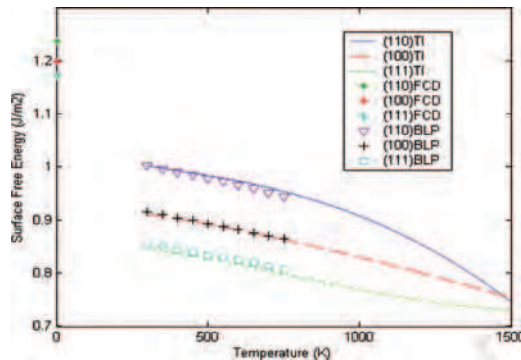


Fig. 3. Solid surface free energies vs temperature for the (111), (100), and (110) faces obtained using the thermodynamic integration technique and the lambda integration method. Also shown are L. Vitos et al.'s FCD results at 0 K. (Picture redrawn from Ref. 17)

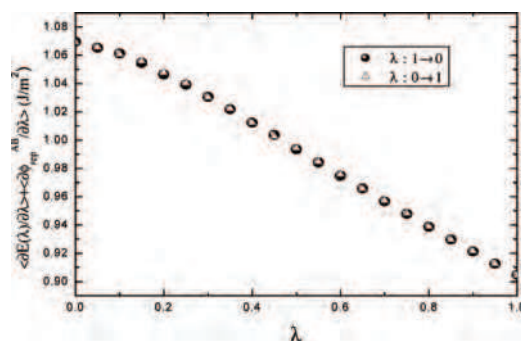


Fig. 4. Simulation results for the integrand $\langle \partial E(\lambda) / \partial \lambda \rangle_\lambda + \langle \partial \varphi_{\text{rep}}^{\text{AB}} / \partial \lambda \rangle_\lambda$ for the (110) face at 750 K. (Picture redrawn from Ref. 17)

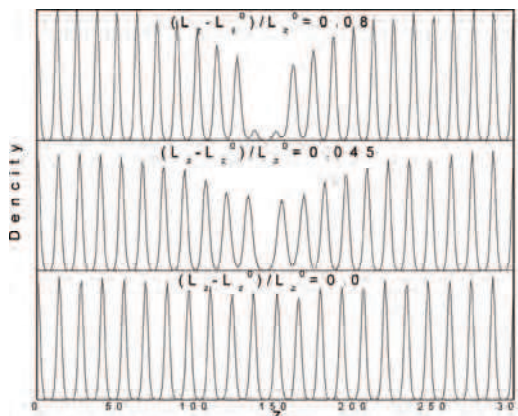


Fig. 5. z density plots for the expansion part of Grochola et al.'s “blanket lambda” path at $(L_z - L_z^0) / L_z^0 = 0, 0.045,$ and 0.08 applied to the (110) face at a temperature of 750 K. (Picture redrawn from Ref. 17)

The calculated average solid surface free energy is shown in Fig. 6. Also shown are the liquid surface free energies and their linear fitting values, $\gamma_L(T) = 0.5773 - 2.3051 \times 10^{-4}(T - 1243)$. At melting point, we acquire the solid surface free energy and the liquid surface free-energy values of 0.793 J/m^2 and 0.577 J/m^2 , respectively. The semi-theoretical estimates of Tyson and Miller²⁸ for the solid surface energy at T_{mb} are $1.086 \text{ (J/m}^2)$, and the experimental value²⁹ for the surface energy of the solid and the liquid states at T_{mb} are 1.205 and $0.903 \text{ (J/m}^2)$, respectively. It should be emphasized that surface free energies of crystalline metals are notoriously difficult to measure and the spread in experimental values for well-defined low-index orientations is substantial, as Bonzel et al.³⁰ pointed out.

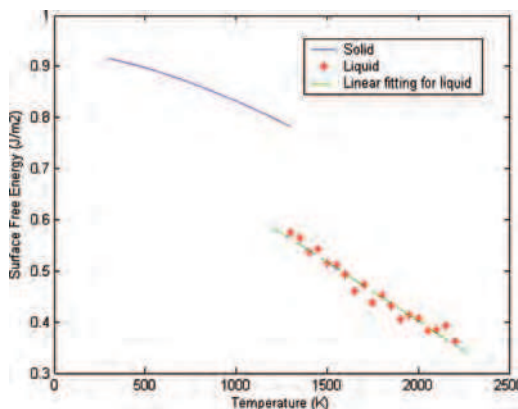


Fig. 6. Surface free energy of the solid and liquid phase in units of J/m^2 as a function of temperature. The data for liquid surface free energy is fitted to a linear function of temperature. (Picture redrawn from Ref. 17)

It is obvious that because MAEAM is developed using only bulk experimental data, it underestimates surface free energy in both the solid and the liquid states as many EAM models do.^{31,32} Though there is the difference between the present results and experimental estimates, we note that the surface free-energy difference between the solid and liquid phase is $0.216 \text{ (J/m}^2\text{)}$ and is between Tyson and Miller's result of $0.183 \text{ (J/m}^2\text{)}$ and the experimental value of $0.3 \text{ (J/m}^2\text{)}$. Furthermore, the average temperature coefficient of the solid and liquid phase surface free energy is $1.32 \times 10^{-4} \text{ (J/m}^2\text{K)}$ and $2.3 \times 10^{-4} \text{ (J/m}^2\text{K)}$, respectively. Such values compare reasonably well with Tyson and Miller's estimate of $1.3 \times 10^{-4} \text{ (J/m}^2\text{K)}$ ²⁸ for the solid and the experimental results of $1.6 \times 10^{-4} \text{ (J/m}^2\text{K)}$ ³³ for the liquid. Therefore, we expect the model to be able to predict the melting points of nanoparticles by means of determining the intersection of free-energy curves. Because the liquid surface free energy is lower than the solid surface free energy, the solid and liquid free-energy curves of nanoparticles change differently when the size of the nanoparticle decreases so that the melting points of nanoparticles decrease with decreasing particle size, as is depicted by Fig. 7. This indicates actually that the surface free-energy difference between the solid and liquid phase is a decisive factor for the size-dependent melting of nanostructural materials.

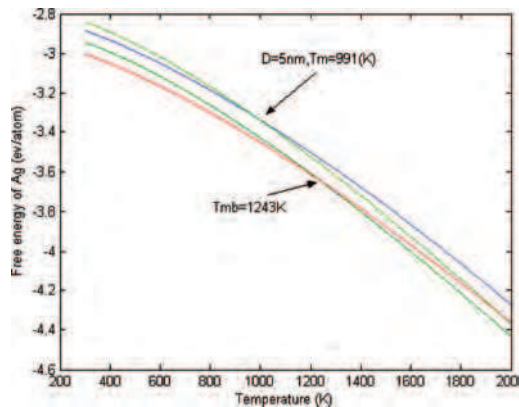


Fig. 7. Gibbs free energies of the solid and liquid phase in units of eV/atom for the bulk material and 5 nm nanoparticle. (Picture redrawn from Ref. 17)

In order to test our model, we plotted the results for the melting temperature versus inverse of the particle diameter in Fig. 8. Because there is no experimental data available for the melting of Ag nanoparticles, the predictions of Nanda et al.¹⁰ and Yang et al.'s³⁴ theoretical model are shown in Fig. 8 for comparison. It can be seen that agreement between our model and Nanda et al.'s¹⁰ theoretical predictions for Ag nanoparticles is excellent. The nonlinear character of the calculated melting curve results from the temperature dependence of the surface free-energy difference between the solid and liquid phase, which is neglected in Nanda et al.'s¹⁰ model. Alternatively, Yang et al.'s³⁴ theoretical predictions may overestimate the melting point depression of Ag nanoparticles.

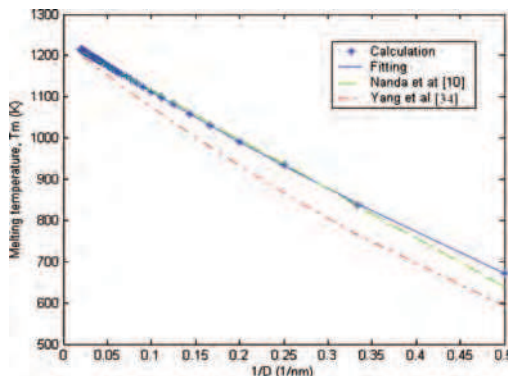


Fig. 8. Melting point vs the reciprocal of nanoparticle diameter. The solid line is the fitting result. The dashed line is the result calculated from the thermodynamic model $T_m = T_{mb}(1 - \beta/d)$,¹⁰ ($\beta = 0.96564$). (Picture redrawn from Ref. 17)

It is believed that understanding and predicting the melting temperature of nanocrystals is important. This is not only because their thermal stability against melting is increasingly becoming one of the major concerns in the upcoming technologies^{1,34,35} but also because many physical and chemical properties of nanocrystals follow the exact same dependence on the particle sizes as the melting temperature of nanocrystals does. For example, the size-dependent volume thermal expansion coefficient, the Debye temperature, the diffusion activation energy, the vacancy formation energy, and the critical ferromagnetic, ferroelectric, and superconductive transition temperature of nanocrystals can be modeled in a fashion similar to the size-dependent melting temperature.^{34,36,37} However, Lai et al.³⁸ pointed out that in order to understand the thermodynamics of nanosized systems comprehensively an accurate experimental investigation of “the details of heat exchange during the melting process, in particular the latent heat of fusion” is required. Allen and co-workers developed a suitable experimental technique to study the calorimetry of the melting process in nanoparticles and found that both the melting temperature and the latent heat of fusion depend on the particle size.³⁸⁻⁴⁰ Here we calculate the molar heat of fusion and molar entropy of fusion for Ag nanoparticles, and the results are shown in Fig. 9. It can be seen that both the molar heat and entropy of fusion undergo a nonlinear decrease as the particle diameter D decreases. In analogy with the melting point, Figure 9 shows that the system of smallest size possesses the lowest latent heat of fusion and entropy of fusion. In a particle with a diameter of 2.5 nm or smaller, all of the atoms should indeed suffer surface effects, and the latent heat of fusion and the entropy of fusion are correspondingly expected to vanish. It is also observed that the size effect on the thermodynamic properties of Ag nanoparticles is not really significant until the particle is less than about 20 nm.

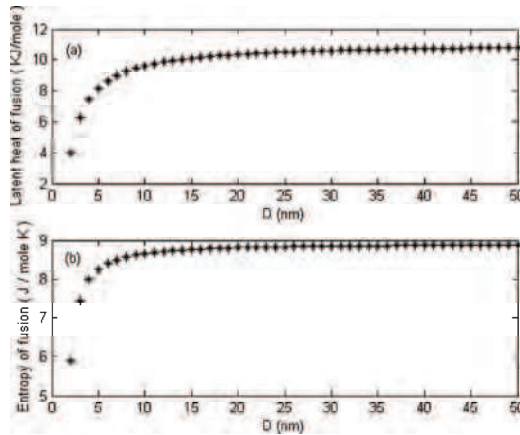


Fig. 9. (a) Molar latent heats of fusion ΔH_m and (b) molar entropy of fusion ΔS_m of Ag nanoparticles as a function of particle diameter D . (Picture redrawn from Ref. 17)

Figure 10 plots the molar heat capacities as a function of temperature for bulk material and nanoparticles. One can see that the molar heat capacity of nanoparticles increases with increasing temperature, as the bulk sample does. The temperature dependence of molar heat capacity qualitatively coincides with that observed experimentally. Figures 10 and 11 show that the molar heat capacity of bulk sample is lower compared to the molar heat capacity of the nanoparticles, and this difference increases with the decrease of particle size. The discrepancy in heat capacities of the nanoparticles and bulk samples is explained in terms of the surface free energy. The molar heat capacity of a nanoparticle consists of the contribution from the bulk and surface region, and the reduced heat capacity C/C_b (C_b denotes bulk heat capacity) varies inversely with the particle diameter D . Likhachev et al.⁴¹ point out that the major contribution to the heat capacity above ambient temperature is determined by the vibrational degrees of freedom, and it is the peculiarities of surface phonon spectra of nanoparticles that are responsible for the anomalous behavior of heat capacity. This is in accordance with our calculation. Recently, Li and Huang⁴² calculated the heat capacity of an Fe nanoparticle with a diameter around 2 nm by using MD simulation and obtained a value of 28J/mol K, which is higher than the value of 25.1J/mol K²² for the bulk solid. It might be a beneficial reference data for understanding the surface effect on the heat capacity of nanoparticles. The ratio $C/C_b=1.1$ they obtained for 2 nm Fe nanoparticles is comparative to our value of 1.08 for 2 nm Ag nanoparticles. Because we set up a spherical face by three special low-index surfaces, the molar heat capacity of nanoparticles necessarily depends on the shape of the particle.

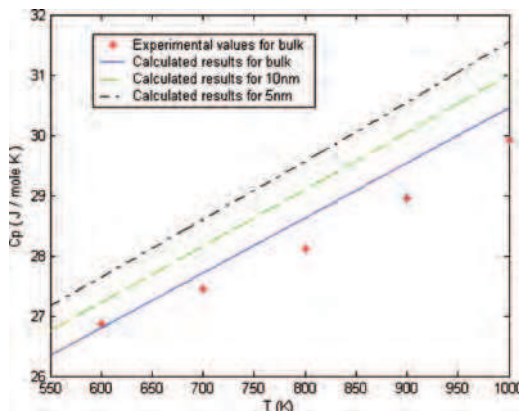


Fig. 10. Molar heat capacity as a function of temperature for Ag nanoparticles and bulk sample. (Picture redrawn from Ref. 17)

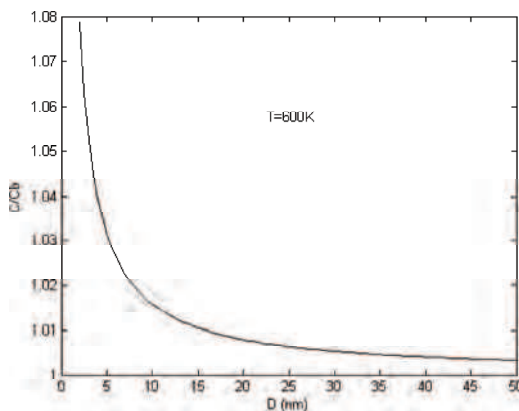


Fig. 11. Dependence of heat capacities of Ag nanoparticles with different sizes relative to the bulk sample. C_b is the heat capacity of the bulk sample. (Picture redrawn from Ref. 17)

The molar entropy as a function of temperature is shown in Fig. 12. It can be seen that the calculated molar entropies are in good agreement with experimental values.²² The molar entropy of nanoparticles is higher than that of the bulk sample, and this difference increases with the decrease of the particle size and increasing temperature. According to Eq. 7, the reduced molar entropy S/S_b (S_b denotes bulk entropy) also varies inversely with the particle diameter D , just as the heat capacity of a nanoparticle does. Because entropy is only related to the first derivatives of Gibbs free energy with regard to temperature, and we have obtained the average temperature coefficient of solid surface energy agreeing with the value in literature,²⁸ it may be believed that Fig. 12 rightly reveals the molar entropy of nanoparticles.

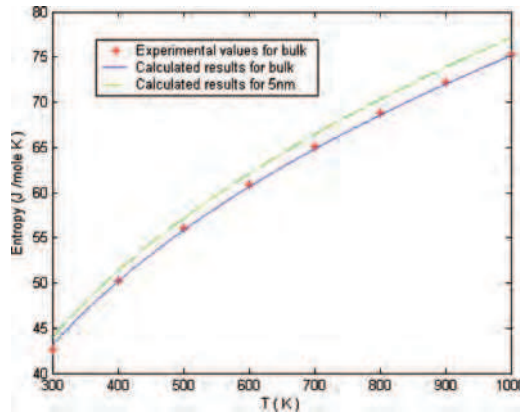


Fig. 12. Molar entropy as a function of temperature for Ag nanoparticles and bulk material. (Picture redrawn from Ref. 17)

2. Grain growth of nanocrystalline silver

Nanocrystalline materials are polycrystalline materials with mean grain size ranging from 1 to 100 nm. Affected by its unique structural characteristics, nano-sized grains and high fraction of grain boundary, nanocrystalline materials possess a series of outstanding physical and chemical properties, especially outstanding mechanical properties, such as increased strength/hardness and superplastic⁴³. However, just because of the high ratio of grain boundary, the nanocrystalline materials usually show low structural stability, the grain growth behavior directly challenges the processing and application of nanocrystalline materials. How to improve the thermal stability of nanocrystalline materials became a challenging study.

Since the network of grain boundary (GB) in a polycrystalline material is a source of excess energy relative to the single-crystalline state, there is a thermodynamic driving force for reduction of the total GB area or, equivalently, for an increase in the average grain size⁴⁴. Especially as grain size decreases to several nanometers, a significant fraction of high excess energy, disordered GB regions in the nanostructured materials provide a strong driving force for grain growth according to the classic growth theory⁴⁵. In contrast to the microcrystal, recent theoretical and simulation studies indicate that grain boundary motion is coupled to the translation and rotation of the adjacent grains⁴⁶. How Bernstein found that the geometry of the system can strongly modify this coupling⁴⁷. We simulate the grain growth in the fully 3D nanocrystalline Ag. It is found that during the process of grain growth in the nanocrystalline materials, there simultaneously exist GB migrations and grain rotation movements^{46,48,49}. The grain growth of nanocrystalline Ag exhibits a Power law growth, followed by a linear relaxation process, and interestingly the dislocations (or stacking faults) play an important intermediary role in the grain growth of nanocrystalline Ag.

For conventional polycrystalline materials, the mechanism of grain growth is GB curvature-driven migration⁴⁴. Recently, the grain rotation mechanism has been found both in the experiments and simulations^{46,48,49}. These two mechanisms are also found in our

simulations as illustrated in Fig. 13 and Fig. 14, respectively. Fig. 13 shows the GB migration in a section perpendicular to Z-axis in the course of grain growth for the 6.06 nm sample at 1000 K. It is clear that the grain 1, as a core, expands through GB migrating outwards until the whole nanocrystal closes to a perfect crystal. Fig. 14 shows the atomic vector movement in the same section as in Fig.13 from 200ps to 320ps, the grain 1 and grain 2 reveal obvious rotation, although these two grains don't coalesce fully by their rotations.

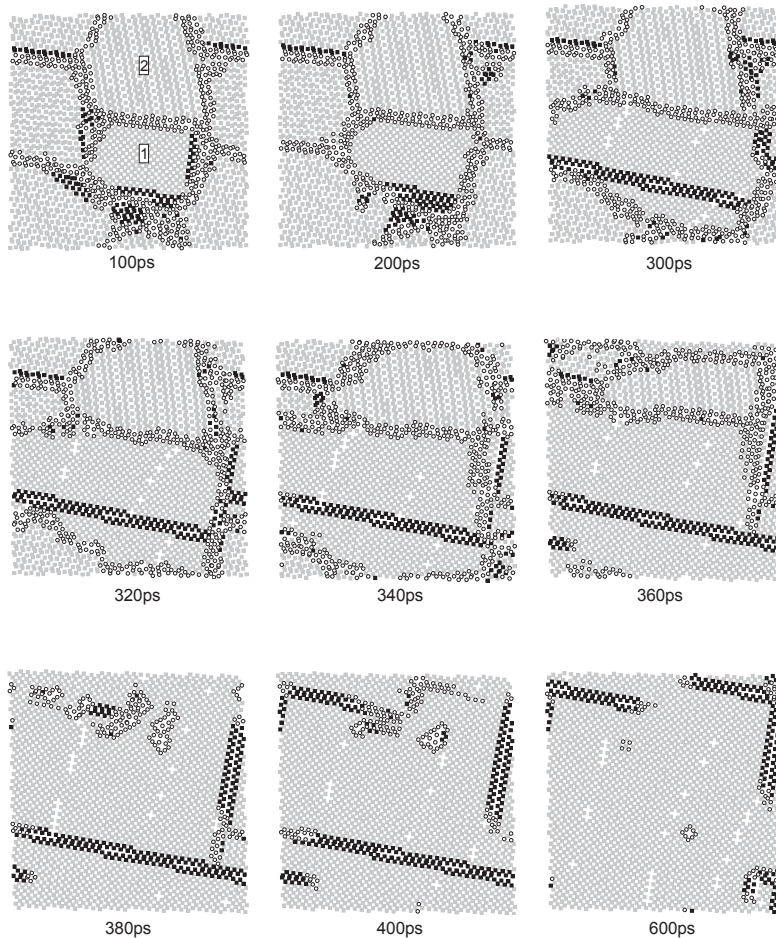


Fig. 13. The typical structural evolution of a section perpendicular to Z-axis during grain growth by GB migration for the 6.06nm specimen at 1000K, the grey squares represent FCC atoms, the black squares for HCP atoms and the circles for the other type atoms, respectively. (Picture redrawn from Ref. 48)

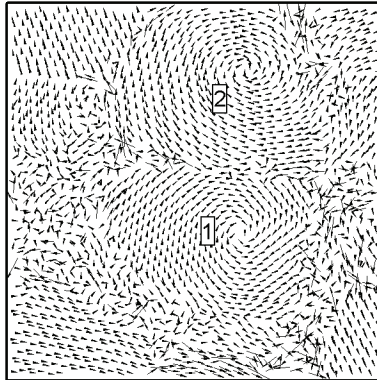


Fig. 14. Atomic vector movement in the same section as in Fig.3 from 200ps to 320ps, the grains 1 and 2 exhibit obvious rotations. (Picture redrawn from Ref. 48)

Figure 15 shows the quantitative evolution of FCC atoms for the 6.06 nm sample at 900 K and 1000 K, respectively. Affected by thermally activated defective atoms at the beginning of imposing thermostat, the number of atoms with FCC structure decreases with the relaxation time (as triangle symbols shown in Fig. 15). Subsequently the grains begin to grow up. It is evident that the process of grain growth can be described as a Power law growth, followed by a linear relaxation stage. In the Power law growth stage, the growth curves are fitted as follows:

$$C = C_0 + Kt^n \quad (11)$$

where C is the proportion of FCC atoms, K is a coefficient and n is termed the grain growth exponent, and the fitted values of n are 3.58 and 3.19 respectively for annealing temperature 1000 K and 900 K. The values of n , which indicate their growth speeds, increase with increasing the annealing temperature. In the Power law growth stage, the grain growth is mainly dominated by the GB migration. In the succedent linear relaxation process, the fraction of FCC atoms increases linearly with time, and this increment mostly comes from the conversion of the fault clusters and dislocations (or stacking faults) left by GB migration (as shown in Fig. 13). In addition, it is noted that the change from Power law growth to linear relaxation is overly abrupt, this is because the sampled points in the structural analysis are very limited and there exists a bit of fluctuation in the structural evolution.

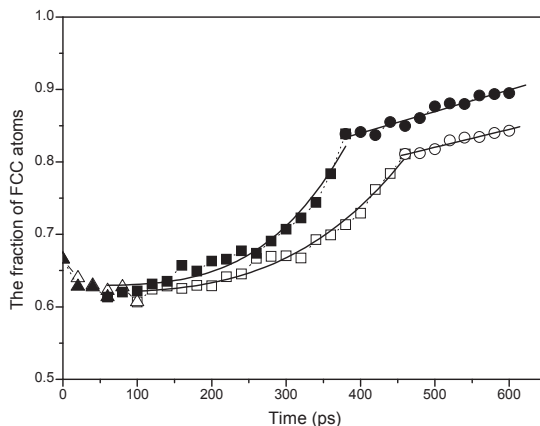


Fig. 15. The isothermal evolution of the fraction of FCC atoms with time for the 6.06nm sample, the solid and the open symbols represent the fraction at 1000K and at 900K, respectively. The triangles represent the thermally disordered stage, the squares for the Power law growth stage, and the circles for the linear relaxation process. (Picture redrawn from Ref. 48)

Besides GB migration and grain rotation, the dislocations (or stacking faults) may play an important role in grain growth of FCC nanocrystals. From the structural analysis it is found that along with the grain growth, the fraction of HCP atoms undergoes a transformation from increasing to decreasing. Comparing the evolution of FCC and HCP atoms with time, the critical transformation time from HCP atoms increasing to decreasing with annealing time is in accordance with the turning point from the Power law growth stage to the linear relaxation stage. At the Power law growth stage, dislocations (or stacking default) are induced after the migration of GB (as shown in Fig. 13), and the fraction of HCP atoms increases. Their configuration evolves from the dispersive atoms and their clusters on GB to aggregative dislocations (or stacking faults) as shown in Fig. 16. Turning into the linear relaxation stage, the fraction of HCP atoms decreases with the annealing time gradually, and some dislocations (or stacking defaults) disappear (as shown in Fig. 13 and Fig. 16). Comparing with the interface energy (about 587.1 mJ/m² and 471.5 mJ/m² for the 6.06 nm and 3.03 nm samples, respectively, if supposing grains as spheres and neglecting the triple-junction as well as high-junction GBs), although stacking default energy is very small for Ag (14.1 mJ/m²), the evolutive characteristic of HCP atoms during grain growth is probably correlative with the stacking fault energy, which lowers the activation energy for atoms on GB converting into stacking faults than directly into a portion of grains, so the dislocations (or stacking faults) may act as the intermediary for the atom transforming from GB to grains.

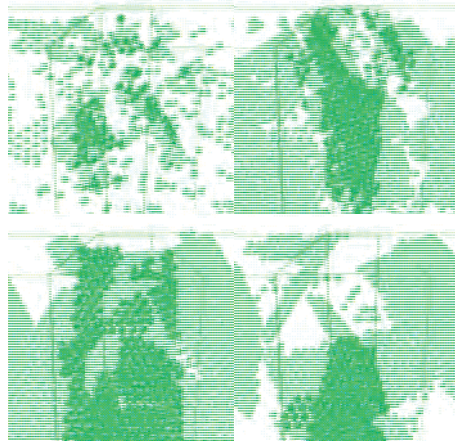


Fig. 16. HCP atoms configuration evolution during grain growth process for the 6.06nm specimen at 1000K. (Picture redrawn from Ref. 48)

3. Melting behaviour of Nanocrystalline silver

Melting temperature (T_m) is a basic physical parameter, which has a significant impact on thermodynamic properties. The modern systematic studies have provided a relatively clear understanding of melting behaviors, such as surface premelting^{50,51}, defect-nucleated microscopic melting mechanisms⁵², and the size-dependent T_m of the low dimension materials¹⁰. In recent years, the unusual melting behaviors of nanostructures have attracted much attention. On a nanometer scale, as a result of elevated surface-to-volume ratio, usually the melting temperatures of metallic particles with a free surface decrease with decreasing their particle sizes^{7,35}, and their melting process can be described as two stages, firstly the stepwise premelting on the surface layer with a thickness of 2-3 perfect lattice constant, and then the abrupt overall melting of the whole cluster.⁵³ For the embedded nanoparticles, their melting temperatures may be lower or higher than their corresponding bulk melting temperatures for different matrices and the epitaxy between the nanoparticles and the embedding matrices⁵⁴. Nanocrystalline (NC) materials, as an aggregation of nano-grains, have a structural characteristic of a very high proportion of grain boundaries (GBs) in contrast to their corresponding conventional microcrystals. As the mean grain size decreases to several nanometers, the atoms in GBs even exceed those in grains, thus, the NC materials can be regarded as composites composed by grains and GBs with a high excess energy. If further decreasing the grain size to an infinitesimal value, at this time, the grain and GB is possibly indistinguishable. What about its structural feature and melting behavior? We have reported on the investigation of the melting behavior for "model" NC Ag at a limited grain-size and amorphous state by means of MD simulation, and give an analysis of thermodynamic and structural difference between GB and amorphous state.^{55,56} Figure 17 shows the variation of T_m of NC Ag and the solid-to-liquid transformation temperature of amorphous state Ag. It can be seen that, from grain-size-varying nanocrystal

to the amorphous, the curve of T_m exhibits three characteristic regions named I, II and III as illustrated in Fig. 17. In addition, considering the nanocrystal being an aggregation of nanoparticles, the T_m of nanoparticles with FCC crystalline structure is appended in Fig. 17.

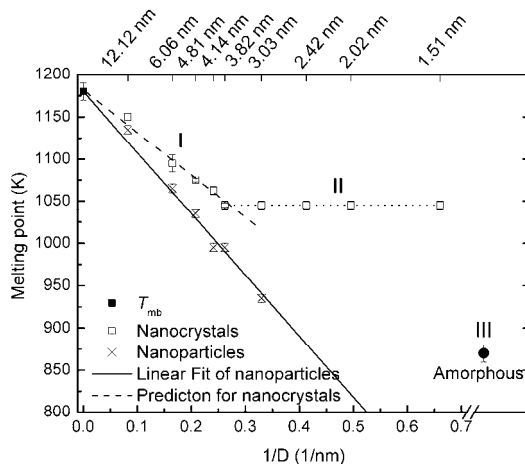


Fig. 17. Melting temperature as a function of the mean grain size for nanocrystalline Ag and of the particle size for the isolated spherical Ag nanoparticles with FCC structure, and the solid-to-liquid transformation temperature of amorphous state. (Picture redrawn from Ref. 56)

In region I, in comparison to T_m (bulk) = 1180 ± 10 K simulated from the solid-liquid coexistence method with same modified analytical embedded atom method (MAEAM) potential, the melting temperatures of the NC Ag are slightly below T_m (bulk) and decrease with the reduction of the mean grain size. This behavior can be interpreted as the effects of GBs on T_m of a polycrystal. MD simulations on a bicrystal model have shown that an interfacial melting transition occurs at a temperature distinctly lower than T_m (bulk) and the width of interfacial region behaving like a melt grows significantly with temperature⁵⁷. This will induce the grains in a polycrystal melted at a temperature lower than T_m (bulk) when the mean grain size decreases to some extent and results in the depression of T_m for the NC materials.

Comparing with the corresponding nanoparticle with the same size, the NC material has a higher T_m . This is to be expected since the atoms on GB are of larger coordination number than those on a free surface, and the interfacial energy (γ_{GB}) is less than the surface energy (γ_{Sur}). It is well known that the main difference between the free particles and the embedded particles or grains in a polycrystal is the interfacial atomic structure. A thermodynamic prediction of T_m from a liquid-drop model¹⁰ for free particles was proposed as follows

$$T_m = T_{mb}(1 - (\beta / d)) \tag{12}$$

where T_{mb} is the melting temperature for conventional crystal, β is a parameter relative to

Thank You for previewing this eBook

You can read the full version of this eBook in different formats:

- HTML (Free /Available to everyone)
- PDF / TXT (Available to V.I.P. members. Free Standard members can access up to 5 PDF/TXT eBooks per month each month)
- Epub & Mobipocket (Exclusive to V.I.P. members)

To download this full book, simply select the format you desire below

